

# Modeling and Bayesian Parameter Estimation for Semibatch pH-Shift Reactive Crystallization of L-Glutamic Acid

Qing-Lin Su and Min-Sen Chiu

Dept. of Chemical and Biomolecular Engineering, National University of Singapore, Singapore 117585, Singapore

Richard D. Braatz

Dept. of Chemical Engineering, Massachusetts Institute of Technology, Cambridge, MA 02139

DOI 10.1002/aic.14481

Published online May 8, 2014 in Wiley Online Library (wileyonlinelibrary.com)

*A mathematical model for semibatch pH-shift reactive crystallization of L-glutamic acid is developed that takes into account the effects of protonation and deprotonation in the species balance of glutamic acid, crystal size distribution, polymorphic crystallization, and nonideal solution properties. The crystallization mechanisms of  $\alpha$ - and  $\beta$ -forms of glutamic acid are addressed by considering primary and secondary nucleation, size-dependent growth rate, and mixing effects on nucleation. The kinetic parameters are estimated by Bayesian inference from batch experimental data collected from literature. Probability distributions of the estimated parameters in addition to their point estimates are obtained by Markov Chain Monte Carlo simulation. The first-principles model is observed in good agreement with the experimental data and can be further used for model predictions in robust control strategies. © 2014 American Institute of Chemical Engineers AIChE J, 60: 2828–2838, 2014*

*Keywords: modeling, Bayesian inference, Markov chain Monte Carlo, semibatch, reactive crystallization*

## Introduction

Crystallization is a separation and purification process widely used in fine chemical, pharmaceutical, and food industries, where high purity is one of the main requirements of the crystalline products. In addition to molecular purity, control of polymorphic purity, crystal size distribution (CSD), and enantiomeric purity are of increasing interest. The crystallization of small-volume and high-value-added products are usually operated in batch or semibatch mode.<sup>1,2</sup>

The supersaturation defined as the difference between the solute concentration and solute solubility is usually treated as the driving force for crystallization processes.<sup>3</sup> Three common ways to generate supersaturation are by cooling, antisolvent addition, and chemical reaction. In cooling and antisolvent crystallization, supersaturation results from reducing the solute solubility to be lower than the solute concentration by decreasing the solution temperature and adding antisolvent to the solution, respectively. For reactive crystallization, supersaturation is created from increasing the solute concentration above the solute solubility by generating more solute through reaction.

In semibatch pH-shift reactive crystallization, acid or base solution is continuously pumped into the crystallizer, which is initially filled with saturated solution, to induce chemical reactions that transform a high soluble solute into a less soluble solute which then precipitates from the supersaturated solution. Although pH-shift reactive crystallization is commonly used in industrial practice for producing amphoteric compounds, such

as amino acids, mathematical modeling of this process remains largely open in the literature.<sup>4,5</sup> The most sophisticated mathematical model for a pH-shift reactive crystallization that has been published is that of Borissova et al.,<sup>6</sup> which used L-glutamic acid as a model compound. Their model assumed ideal solution properties and a simple empirical power-law kinetic mechanism and did not include polymorphic crystallization phenomena and mixing effects. Here, we develop a more comprehensive mathematical model for pH-shift reactive crystallization that includes these phenomena.

The advantages of using Bayesian estimation over the weighted least squares for parameter estimation are well documented in the literature over the years, including in chemical reactions,<sup>7</sup> heat transfer in packed beds,<sup>8</sup> microbial systems,<sup>9–11</sup> microelectronics processes,<sup>12</sup> and polymorphic crystallization.<sup>13</sup> Here, Bayesian inference is used to quantify uncertainties in the estimates of parameters in the mathematical model developed in this article.

This article is organized as follows. The next section describes the development of a mathematical model for semibatch pH-shift reactive crystallization process using L-glutamic acid as a model compound. This is followed by the brief introduction of Bayesian inference for model parameter estimation. The results of model parameters estimation obtained using experimental data from literature are discussed, followed by the conclusions.

## Mathematical Model

### Species balance model

For the model compound of L-glutamic acid, the dissolution of monosodium glutamate (MSG) in pure water due to

Correspondence concerning this article should be addressed to R. D. Braatz at braatz@mit.edu or M.-S. Chiu at chems@nus.edu.sg.

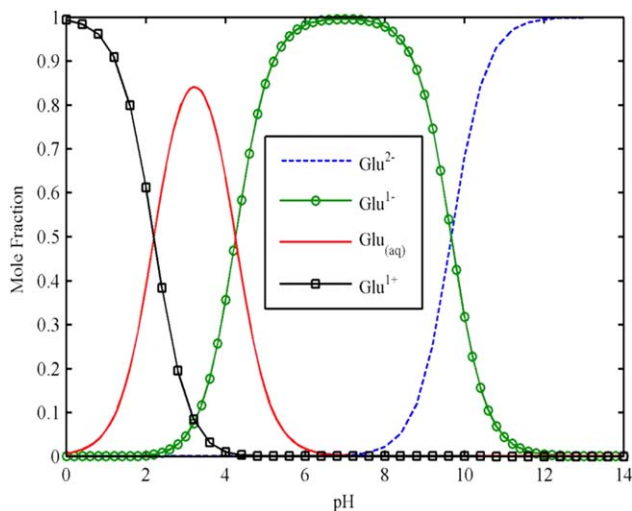
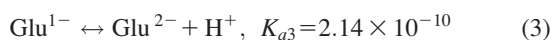
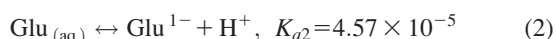
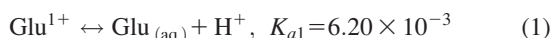


**Figure 1. Mole fractions of different ionic species in the solution as a function of pH.**

[Color figure can be viewed in the online issue, which is available at [wileyonlinelibrary.com](http://wileyonlinelibrary.com).]

protonation and deprotonation mechanism can be represented by<sup>6</sup>



where  $\text{Glu}^{1+}$  is the protonated form with an overall charge of +1;  $\text{Glu}^{1-}$  is the deprotonated form with an overall charge of -1, viz., MSG;  $\text{Glu}^{2-}$  is the fully deprotonated form with an overall charge of -2;  $\text{Glu}_{(\text{aq})}$  and  $\text{Glu}_{(\text{solid})}$  are the GA zwitterion with an overall charge of zero in aqueous solution and solid, respectively;  $K_{ai}$  ( $i = 1, 2, 3$ ) are the respective equilibrium constants; and  $K_{\text{sp}}$  is the solubility product for GA.<sup>14</sup> The four solute-related species can coexist in the solution, which change their respective concentrations or fractions in solution with varying pH, as shown in Figure 1.

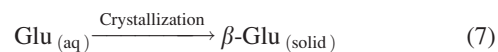
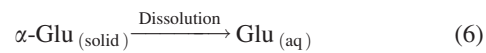
In the experimental system of Ref. 15, the crystallizer was initially filled with MSG solution and then sulfuric acid was continuously pumped into the crystallizer, which produced glutamic acid according to the overall reaction



With continuous addition of the sulfuric acid, decreasing the pH of the solution favors the conversion of sodium glutamate into glutamic acid. However, due to the protonation/deprotonation as indicated in reactions (1)–(3), glutamic acid will be further protonated. For any particular value of the pH within the range of operation, there are always at least two species in the solution as shown in Figure 1.

It is assumed that the species balance for glutamic acid in solution will reach dynamic equilibrium instantaneously when sulfuric acid is added into the crystallizer.<sup>6</sup> For the various species in solution, only the zwitterion glutamic acid precipitates because of its lowest intrinsic solubility. Either or both of two polymorphic forms of glutamic acid, namely, metastable  $\alpha$ -form and stable  $\beta$ -form, can nucleate or grow competitively in solution depending on the solution concentration. As the  $\beta$ -form is more stable, a solution-mediated

polymorphic transformation (SMPT) from metastable  $\alpha$ -form to the stable  $\beta$ -form takes place, when  $C_{\beta}^* < C < C_{\alpha}^*$ , as<sup>15\*</sup>

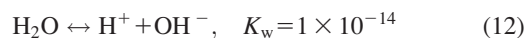
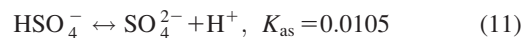
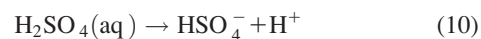


with the intrinsic solubility of two polymorphs given by

$$C_{\alpha}^* = 7.4 \times 10^{-2} \text{ mol/L} \quad (8)$$

$$C_{\beta}^* = 5.6 \times 10^{-2} \text{ mol/L} \quad (9)$$

The dissociations of sulfuric acid and the autoprotolysis of water are also considered



The solution during crystallization conditions has sufficient water that  $\text{H}_2\text{SO}_4$  rapidly dissociates with subsequent formation of  $\text{HSO}_4^-$ . Furthermore, the activity-based equilibrium constant  $K_a = K_c K_{\gamma}$ , where  $K_c$  is the concentration-based equilibrium constant and  $K_{\gamma}$  is computed by activity coefficients, is employed to deal with the nonideal solution properties, which is less restrictive compared to Ref. 6 where ideal solution was assumed. The activity coefficient of electrically neutral glutamic acid,  $\text{Glu}_{(\text{aq})}$ , is assumed to be one. The activity coefficients,  $\gamma_i$ , for other ions are calculated based on the modified Bates–Guggenheim equation with parameter values  $A = 1.175$  and  $B = 0.15$ <sup>15</sup>

$$\ln \gamma_i = -Az_i^2 \frac{\sqrt{I_c}}{1 + 1.5\sqrt{I_c}} + BI_c \quad (13)$$

where  $I_c$  and  $z$  denote the ion strength and ion charge, respectively.

### Population balance model

The crystal size distribution is an important concern in industrial manufacturing, due to its effect on product performance and on downstream processing, such as washing, filtering, drying, and milling.<sup>6</sup> During crystallization, the size distribution can be affected by many factors, such as nucleation, the size distribution of crystal seeds, growth dispersion, breakage, attrition, agglomeration, polymorphism, and changes in morphology.

For a perfectly mixed batch crystallizer, in which it is assumed that (a) crystal nuclei are of negligible size, (b) crystal breakage and agglomeration are negligible, and (c) the crystal shape is uniform, the crystal size distribution can be expressed as the distribution of the number of crystals over the size range, as characterized by the population balance equation

$$\frac{\partial(n_i(L, t)V)}{\partial t} + \frac{\partial(G_i(S_i, L)n_i(L, t)V)}{\partial L} = 0, \quad i = \alpha, \beta \quad (14)$$

where  $L$  is the characteristic length of the  $i$  polymorphic form of glutamic acid,  $m$ ;  $n_i$  is the number density<sup>†</sup> of the  $i$  polymorphic form,  $\#/m^4$ ;  $V$  is the solution volume,  $m^3$ ; and

\*The mathematical model implements SMPT as two kinetic steps, which are the dissolution of  $\alpha$ -form and the growth of  $\beta$ -form, which are given in the following subsection.

†The number density is the number of crystals of  $i$  polymorphic form per unit volume in between size  $L$  and  $L + dL$ .

$G_i$  is the growth rate of the  $i$  polymorphic form, m/s. Because the solution volume of a semibatch crystallizer is time varying, it is convenient to redefine the number density on the basis of the total operating volume of the system such that<sup>6,16</sup>

$$f_i = n_i V \quad (15)$$

$$\frac{\partial f_i}{\partial t} + \frac{\partial(G_i f_i)}{\partial L} = 0 \quad (16)$$

where  $f_i$  is the number density over the total solution volume, #/m, and the boundary conditions are

$$f_i(L, 0) = \begin{cases} 0, & \text{for an unseeded crystallization} \\ f_{\text{seed},i}(L), & \text{for a seeded crystallization} \end{cases} \quad (17)$$

$$f_i(0, t) = f_{i,\text{in}} \quad (18)$$

where  $f_{\text{seed},i}(L)$  is the size distribution of crystal seeds for the  $i$  polymorphic form and  $f_{i,\text{in}}$  is the population density of nuclei for the  $i$  polymorphic form at size zero, which can be obtained from

$$f_{i,\text{in}} = \frac{B_i V}{G_i} \quad (19)$$

where  $B_i$  is the nucleation rate of the  $i$  polymorphic form, #/m<sup>3</sup>/s.

Based on the crystal size distribution, the average length, total number, surface, volume, and mass of the crystals can be computed from the  $n$ th moments of the size distribution

$$\mu_{i,n} = \int_0^{\infty} L^n f_i dL, \quad n=0, 1, 2, 3, \dots \quad (20)$$

where  $\mu_{i,0}$  is the total number of crystals for the  $i$  polymorphic form in the crystallizer,  $\mu_{i,1}$  is the total length,  $\mu_{i,1}/\mu_{i,0}$  is the number-averaged length,  $\mu_{i,2}$  is proportional to the total surface area, and  $\mu_{i,3}$  is proportional to the total volume of the crystals.

The total concentration of the various glutamic ions,  $C_{\text{T,Glu}}$ , links the species balance and population balance models together

$$C_{\text{T,Glu}} = C_{\text{Glu}^{2-}} + C_{\text{Glu}^{1-}} + C_{\text{Glu}(\text{aq})} + C_{\text{Glu}^{1+}} \quad (21)$$

$$C_{\text{T,Glu}} = \frac{C_{\text{T,Glu}}^0 V_0}{V} - \frac{\rho_{\alpha} k_{v\alpha} (\mu_{\alpha,3} - \mu_{\alpha,3}^0) + \rho_{\beta} k_{v\beta} (\mu_{\beta,3} - \mu_{\beta,3}^0)}{\text{MW}_{\text{Glu}} V} \quad (22)$$

where  $C_{\text{T,Glu}}^0$  is the initial total concentration of various glutamic species,  $V_0$  is the initial solution volume,  $\rho_i$  is the density of glutamic acid of the  $i$  polymorphic form,  $k_{vi}$  is the volumetric shape factor of the  $i$  polymorphic form,  $\mu_{i,3}^0$  is the initial 3rd moment of the  $i$  polymorphic form, and  $\text{MW}_{\text{Glu}}$  is the molecular weight of glutamic acid.

### Crystallization mechanisms and kinetics

The crystallization mechanism includes nucleation and crystal growth, which are both driven by supersaturation. In this context, for a highly saturated solution during a pH-shift reactive crystallization, it is appropriate to use the relative supersaturation definition<sup>17-19</sup>

$$S_i = \frac{C}{C_i^*}, \quad i = \alpha, \beta \quad (23)$$

This study considers both primary and secondary nucleation of  $\alpha$ - and  $\beta$ -forms and the effect of mixing intensity,  $I$ , is also taken into account in the nucleation. Furthermore, the effect of  $\alpha$ -form crystals on the secondary nucleation of  $\beta$ -form crystals was also considered, to take into account that  $\beta$ -form crystals can nucleate from the surface of  $\alpha$ -form crystals.<sup>13</sup> The growth and nucleation expressions are assumed to have similar dependencies on supersaturation as reported in past studies,<sup>20,21</sup> with a length-dependent term included in the crystal growth kinetic expression. The expressions for the crystallization kinetics are:

$\alpha$ -form crystallization kinetics when  $S_{\alpha} > 1$

$$B_{\alpha} = k_{b,\alpha 1} (\ln S_{\alpha})^{b_{\alpha,1}} \exp\left(-\frac{E_{b,\alpha 2}}{(\ln S_{\alpha})^2}\right) I^{b_{\alpha,2}} + k_{b,\alpha 2} m_{\alpha}^{b_{\alpha,3}} (\ln S_{\alpha})^{b_{\alpha,4}} I^{b_{\alpha,5}} \quad (24)$$

$$k_{b,\alpha 1} = k_{b,\alpha 0} \exp\left(-\frac{E_{b,\alpha 1}}{RT}\right) \quad (25)$$

$$G_{\alpha} = k_{g,\alpha 1} (\ln S_{\alpha})^{g_{\alpha,1}} \exp\left(-\frac{E_{g,\alpha 2}}{\ln S_{\alpha}}\right) \exp\left(-\frac{L}{L_{\alpha,0}}\right) \quad (26)$$

$$k_{g,\alpha 1} = k_{g,\alpha 0} \exp\left(-\frac{E_{g,\alpha 1}}{RT}\right) \quad (27)$$

$\beta$ -form crystallization kinetics when  $S_{\beta} > 1$

$$B_{\beta} = k_{b,\beta 1} (\ln S_{\beta})^{b_{\beta,1}} \exp\left(-\frac{E_{b,\beta 2}}{(\ln S_{\beta})^2}\right) I^{b_{\beta,2}} + (k_{b,\beta 2} m_{\alpha}^{b_{\beta,3}} + k_{b,\beta 3} m_{\beta}^{b_{\beta,4}}) (\ln S_{\beta})^{b_{\beta,5}} I^{b_{\beta,6}} \quad (28)$$

$$k_{b,\beta 1} = k_{b,\beta 0} \exp\left(-\frac{E_{b,\beta 1}}{RT}\right) \quad (29)$$

$$G_{\beta} = k_{g,\beta 1} (\ln S_{\beta})^{g_{\beta,1}} \exp\left(-\frac{E_{g,\beta 2}}{\ln S_{\beta}}\right) \exp\left(-\frac{L}{L_{\beta,0}}\right) \quad (30)$$

$$k_{g,\beta 1} = k_{g,\beta 0} \exp\left(-\frac{E_{g,\beta 1}}{RT}\right) \quad (31)$$

where  $m_i$  is the mass concentration of the  $i$  polymorphic form of glutamic acid in the solution, kg/m<sup>3</sup>;  $L_{i,0}$  is the critical characteristic length of the  $i$  polymorphic form, m;  $R$  is the universal gas constant, 8.314 J/mol/K; and  $T$  is the temperature, K.

The mixing intensity is calculated by<sup>22</sup>

$$I = \frac{N_p D_{\text{imp}}^5 N_s^3}{V} \quad (32)$$

where  $N_p$  is the power number for the stirrer type,  $D_{\text{imp}}$  is the impeller diameter, m, and  $N_s$  is the stirring rate, s<sup>-1</sup>.

Finally, when the solute concentration is below the solubility of the  $\alpha$ -form glutamic acid, the polymorphic transformation from the  $\alpha$ - to  $\beta$ -form may occur through SMPT. Then, it is necessary to consider the dissolution of the  $\alpha$ -form in the kinetic scheme, which is given as<sup>13,22</sup>

$$G_{\alpha} = k_{d,\alpha} (S_{\alpha} - 1), \quad S_{\alpha} \leq 1 \quad (33)$$

where  $k_{d,\alpha}$  is the dissolution rate constant. The dissolution of  $\beta$ -form is avoided after the crystallization occurs, and so is not considered in this study.

## Numerical solution

The mathematical model combining all the above equations consists of partial differential equations (PDEs), ordinary differential equations (ODEs), and nonlinear algebraic equations that need to be solved simultaneously. To obtain the crystal size distribution of both polymorphs, numerical techniques that reduce the PDEs into ODEs by discretization of the length axis are common choices. The high-resolution finite-volume method with second-order accuracy and flux-limiting functions<sup>23</sup> was used here. The characteristic crystal length  $L$  was first discretized as shown in Figure 2, which is the same as in the standard finite-volume method. The equations obtained after discretization are<sup>23–25</sup>

if  $GL_i^+ \geq 0$

$$\text{if } i=0: (Gf)_{1/2} = G_{in}f_{in,0}$$

$$\text{if } i=1: (Gf)_{3/2} = G_{3/2} \left( \frac{f_1 + f_2}{2} \right)$$

$$\text{if } i=N: (Gf)_{N+1/2} = G_{N+1/2} \left( f_N + \frac{f_N - f_{N-1}}{2} \right)$$

$$\text{else: } (Gf)_{L_i^+} = G_{L_i^+} \left[ f_i + \frac{1}{2} \varphi(\gamma_i^+) (f_i - f_{i-1}) \right]$$

$$\gamma_i^+ = \frac{f_{i+1} - f_i + \varepsilon}{f_i - f_{i-1} + \varepsilon}, \varepsilon = 1 \times 10^{-10}$$

$$\frac{df_i}{dt} + \frac{(Gf)_{L_i^+} - (Gf)_{L_i^-}}{L_i^+ - L_i^-} = 0$$

else

$$\text{if } i=0: (Gf)_{1/2} = G_{1/2} \left[ f_1 + \frac{f_1 - f_2}{2} \right]$$

$$\text{if } i=N-1: (Gf)_{N-1/2} = G_{N-1/2} \frac{f_N + f_{N-1}}{2}$$

$$\text{if } i=N: (Gf)_{N+1/2} = G_{in}f_{in, N}$$

$$\text{else: } (Gf)_{L_i^+} = G_{L_i^+} \left[ f_{i+1} + \frac{1}{2} \varphi(\gamma_i^+) (f_{i+1} - f_{i+2}) \right]$$

$$\gamma_i^+ = \frac{f_i - f_{i+1} + \varepsilon}{f_{i+1} - f_{i+2} + \varepsilon}, \varepsilon = 1 \times 10^{-10}$$

$$\frac{df_i}{dt} + \frac{(Gf)_{L_i^-} - (Gf)_{L_i^+}}{L_i^- - L_i^+} = 0$$

end

$$\text{where } \varphi(\gamma_i^+) = \max \left\{ 0, \min \left\{ 2\gamma_i^+, \min \left\{ \frac{1}{3} + \frac{2}{3}\gamma_i^+, 2 \right\} \right\} \right\}.$$

Using the MATLAB ODE solver *ode45*, these ODEs were solved simultaneously with the conservation equations

$$\frac{dV}{dt} = F \quad (34)$$

$$\frac{dC_{T,Glu}}{dt} = -\frac{C_{T,Glu}}{V} \frac{dV}{dt} \quad (35)$$

$$\frac{dC_{Na^+}}{dt} = -\frac{C_{Na^+}}{V} \frac{dV}{dt} \quad (36)$$

$$\frac{dC_{T,S}}{dt} = -\frac{C_{T,S}}{V} \frac{dV}{dt} + \frac{C_{0,S}F}{V} \quad (37)$$

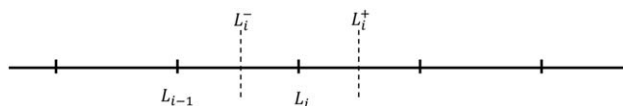


Figure 2. Cell-centered finite-volume grid.

$$C_{T,S} = C_{HSO_4^-} + C_{SO_4^{2-}} \quad (38)$$

where  $F$  is the acid addition flow rate,  $m^3/s$ ;  $C_{Na^+}$  is the concentration of sodium ion,  $mol/m^3$ ;  $C_{T,S}$  is the total concentration of sulfuric related ions,  $mol/m^3$ ; and  $C_{0,S}$  is the concentration of sulfuric acid added into the system,  $mol/m^3$ .

## Bayesian Inference

The parameters in the first-principles model in the last section were determined by Bayesian estimation. A brief summary of Bayesian inference is provided here; for a thorough discussion, readers are referred to the literature.<sup>13,26–28</sup>

The main idea of Bayesian inference lies in Bayes' rule

$$\Pr(\theta|\mathbf{y}) = \frac{\Pr(\mathbf{y}|\theta)\Pr(\theta)}{\Pr(\mathbf{y})} \quad (39)$$

where  $\theta$  is a vector of unknown parameters and  $\mathbf{y}$  is a vector of the observations, such as measurements of state variables at different time points, to be used to infer  $\theta$ .  $\Pr(\theta)$  is the prior distribution of  $\theta$ ,  $\Pr(\mathbf{y}|\theta)$  is referred as the sampling distribution for fixed parameters  $\theta$  and is also referred to as the likelihood function  $L(\theta|\mathbf{y})$  when the data  $\mathbf{y}$  are known and the parameters  $\theta$  are unknown.  $\Pr(\theta|\mathbf{y})$  is referred as the Bayesian posterior distribution of  $\theta$  and  $\Pr(\mathbf{y})$  acts as a normalizing constant to ensure that the Bayesian posterior integrates to unity, which is often neglected as it does not affect the shape of the posterior distribution of  $\theta$ .

When the model structure is assumed correct and the measurement noise is distributed normally with zero mean and unknown variance, then the likelihood function can be characterized as follows<sup>13</sup>

$$\begin{aligned} L(\theta|\mathbf{y}) &= L(\theta_{sys}, \sigma|\mathbf{y}) = \prod_{j=1}^{N_m} \prod_{k=1}^{N_{d_j}} \Pr(y_{jk}|\theta_{sys}, \sigma) \\ &= \prod_{j=1}^{N_m} \prod_{k=1}^{N_{d_j}} \frac{1}{\sqrt{2\pi}\sigma_j} \exp\left(-\frac{(y_{jk} - \hat{y}_{jk}(\theta_{sys}))^2}{2\sigma_j^2}\right) \\ &= \frac{1}{\prod_{j=1}^{N_m} (\sqrt{2\pi}\sigma_j)^{N_{d_j}}} \exp\left(-\sum_{j=1}^{N_m} \sum_{k=1}^{N_{d_j}} \frac{(y_{jk} - \hat{y}_{jk}(\theta_{sys}))^2}{2\sigma_j^2}\right) \end{aligned} \quad (40)$$

where  $\theta = [\theta_{sys}, \sigma]^T$  is the vector of parameters of interest, which consists of the system/model ( $\theta_{sys}$ ) and noise ( $\sigma$ ) parameters,  $y_{jk}$  and  $\hat{y}_{jk}$  are the measurement and predicted value of the  $j$ th variable at sampling instance  $k$ , respectively,  $N_m$  is the number of measured variables,  $N_{d_j}$  is the number of time samples of the  $j$ th variable, and  $\sigma_j$  is the standard deviation of the measurement noise in the  $j$ th variable. This likelihood function assumes that the measurement noises are independent.

**Table 1. Summary of Experimental Data<sup>27,30</sup>**

No.	Reagent Concentration (M)	Mixing Intensity (rpm)	Impeller Type	Measurement Data
E1	0.75	250	Six flat blade disk turbine	pH value <input checked="" type="checkbox"/> Glutamic acid concentration <input type="checkbox"/> Polymorphic mass fraction <input checked="" type="checkbox"/> Crystal size distribution <input checked="" type="checkbox"/>
E2	0.75	500	Six flat blade disk turbine	pH value <input type="checkbox"/> Glutamic acid concentration <input type="checkbox"/> Polymorphic mass fraction <input checked="" type="checkbox"/> Crystal size distribution <input checked="" type="checkbox"/>
E3	1.00	250	Six pitched blade turbine	pH value <input checked="" type="checkbox"/> Glutamic acid concentration <input checked="" type="checkbox"/> Polymorphic mass fraction <input checked="" type="checkbox"/> Crystal size distribution <input type="checkbox"/>
E4	1.00	500	Six pitched blade turbine	pH value <input checked="" type="checkbox"/> Glutamic acid concentration <input type="checkbox"/> Polymorphic mass fraction <input checked="" type="checkbox"/> Crystal size distribution <input type="checkbox"/>
E5	1.25	250	Six flat blade disk turbine	pH value <input checked="" type="checkbox"/> Glutamic acid concentration <input type="checkbox"/> Polymorphic mass fraction <input checked="" type="checkbox"/> Crystal size distribution <input type="checkbox"/>
E6	1.25	500	Six pitched blade turbine	pH value <input checked="" type="checkbox"/> Glutamic acid concentration <input type="checkbox"/> Polymorphic mass fraction <input checked="" type="checkbox"/> Crystal size distribution <input type="checkbox"/>
E7	1.50	250	Six flat blade disk turbine	pH value <input checked="" type="checkbox"/> Glutamic acid concentration <input type="checkbox"/> Polymorphic mass fraction <input checked="" type="checkbox"/> Crystal size distribution <input type="checkbox"/>
E8	1.50	500	Six pitched blade turbine	pH value <input checked="" type="checkbox"/> Glutamic acid concentration <input type="checkbox"/> Polymorphic mass fraction <input checked="" type="checkbox"/> Crystal size distribution <input type="checkbox"/>

Due to the fact that feeding up would cause imperfect mixing, which was inconsistent with the assumption of perfect mixing in the model, this article only considers datasets that used feeding down.

■: Data available.

□: Data unavailable.

**Table 2. Estimated Model Parameters**

	Parameter	Mean	Mode	95% Credible Interval
$\alpha$ nucleation	$k_{b,\alpha 1}$	$9.83 \times 10^{10}$	$9.92 \times 10^{10}$	$(7.20, 12.31) \times 10^{10}$
	$b_{\alpha,1}$	$5.21 \times 10^{-1}$	$5.01 \times 10^{-1}$	$(3.78, 6.75) \times 10^{-1}$
	$E_{b,\alpha 2}$	$1.04 \times 10^1$	$1.04 \times 10^1$	$(0.90, 1.22) \times 10^1$
	$b_{\alpha,2}$	$9.59 \times 10^{-1}$	$9.73 \times 10^{-1}$	$(7.78, 11.40) \times 10^{-1}$
	$k_{b,\alpha 2}$	$6.99 \times 10^7$	$6.74 \times 10^7$	$(5.28, 9.03) \times 10^7$
	$b_{\alpha,3}$	$9.81 \times 10^{-1}$	$9.18 \times 10^{-1}$	$(7.37, 12.40) \times 10^{-1}$
$\alpha$ growth	$b_{\alpha,4}$	$4.93 \times 10^{-1}$	$4.96 \times 10^{-1}$	$(3.43, 6.25) \times 10^{-1}$
	$b_{\alpha,5}$	$9.64 \times 10^{-1}$	$9.96 \times 10^{-1}$	$(6.90, 11.72) \times 10^{-1}$
	$k_{g,\alpha 1}$	$9.68 \times 10^{-7}$	$9.94 \times 10^{-7}$	$(7.43, 11.58) \times 10^{-7}$
	$g_{\alpha,1}$	$4.93 \times 10^{-1}$	$5.16 \times 10^{-1}$	$(3.46, 6.16) \times 10^{-1}$
	$E_{g,\alpha 2}$	$8.27 \times 10^{-1}$	$8.64 \times 10^{-1}$	$(5.43, 10.18) \times 10^{-1}$
	$L_{\alpha,0}$	$10.14 \times 10^{-4}$	$9.91 \times 10^{-4}$	$(7.32, 12.95) \times 10^{-4}$
$\beta$ nucleation	$k_{b,\beta 1}$	$5.03 \times 10^{14}$	$4.86 \times 10^{14}$	$(3.80, 6.30) \times 10^{14}$
	$b_{\beta,1}$	$5.30 \times 10^0$	$4.75 \times 10^0$	$(4.05, 6.91) \times 10^0$
	$E_{b,\beta 2}$	$3.09 \times 10^1$	$3.10 \times 10^1$	$(2.68, 3.63) \times 10^1$
	$b_{\beta,2}$	$1.01 \times 10^0$	$1.02 \times 10^0$	$(0.81, 1.20) \times 10^0$
	$k_{b,\beta 2}$	$7.39 \times 10^7$	$7.15 \times 10^7$	$(5.62, 9.53) \times 10^7$
	$b_{\beta,3}$	$9.75 \times 10^{-1}$	$9.32 \times 10^{-1}$	$(7.61, 11.79) \times 10^{-1}$
	$k_{b,\beta 3}$	$7.63 \times 10^7$	$7.46 \times 10^7$	$(6.09, 9.90) \times 10^7$
	$b_{\beta,4}$	$9.52 \times 10^{-1}$	$9.20 \times 10^{-1}$	$(7.29, 11.68) \times 10^{-1}$
	$b_{\beta,5}$	$9.81 \times 10^{-1}$	$9.71 \times 10^{-1}$	$(7.22, 12.25) \times 10^{-1}$
	$b_{\beta,6}$	$10.02 \times 10^{-1}$	$9.60 \times 10^{-1}$	$(7.16, 13.13) \times 10^{-1}$
$\beta$ growth	$k_{g,\beta 1}$	$1.14 \times 10^{-7}$	$1.10 \times 10^{-7}$	$(0.93, 1.40) \times 10^{-7}$
	$g_{\beta,1}$	$2.69 \times 10^0$	$2.58 \times 10^0$	$(1.97, 3.53) \times 10^0$
	$E_{g,\beta 2}$	$8.70 \times 10^{-1}$	$8.81 \times 10^{-1}$	$(6.67, 10.61) \times 10^{-1}$
	$L_{\beta,0}$	$2.71 \times 10^{-4}$	$2.77 \times 10^{-4}$	$(1.74, 3.49) \times 10^{-4}$
Power number	$N_p^a$	$6.28 \times 10^{-1}$	$6.04 \times 10^{-1}$	$(5.11, 7.84) \times 10^{-1}$
	$N_p^b$	$5.68 \times 10^{-1}$	$5.84 \times 10^{-1}$	$(4.00, 6.89) \times 10^{-1}$
Raman corrections	$m_{Raman}$	$5.08 \times 10^{-1}$	$5.12 \times 10^{-1}$	$(3.63, 6.55) \times 10^{-1}$
Measurement noise	$\sigma_{pH}$	$2.02 \times 10^{-1}$	$1.99 \times 10^{-1}$	$(1.61, 2.46) \times 10^{-1}$
	$\sigma_{ATR-FTIR}$	$1.78 \times 10^{-2}$	$1.78 \times 10^{-2}$	$(1.39, 2.27) \times 10^{-2}$
	$\sigma_{Raman}$	$1.04 \times 10^{-1}$	$1.05 \times 10^{-1}$	$(0.84, 1.29) \times 10^{-1}$
	$\sigma_{CSD}$	$1.46 \times 10^{-3}$	$1.41 \times 10^{-3}$	$(1.11, 1.96) \times 10^{-3}$

<sup>a</sup>Six pitched blade turbine.

<sup>b</sup>Six flat blade disk turbine.

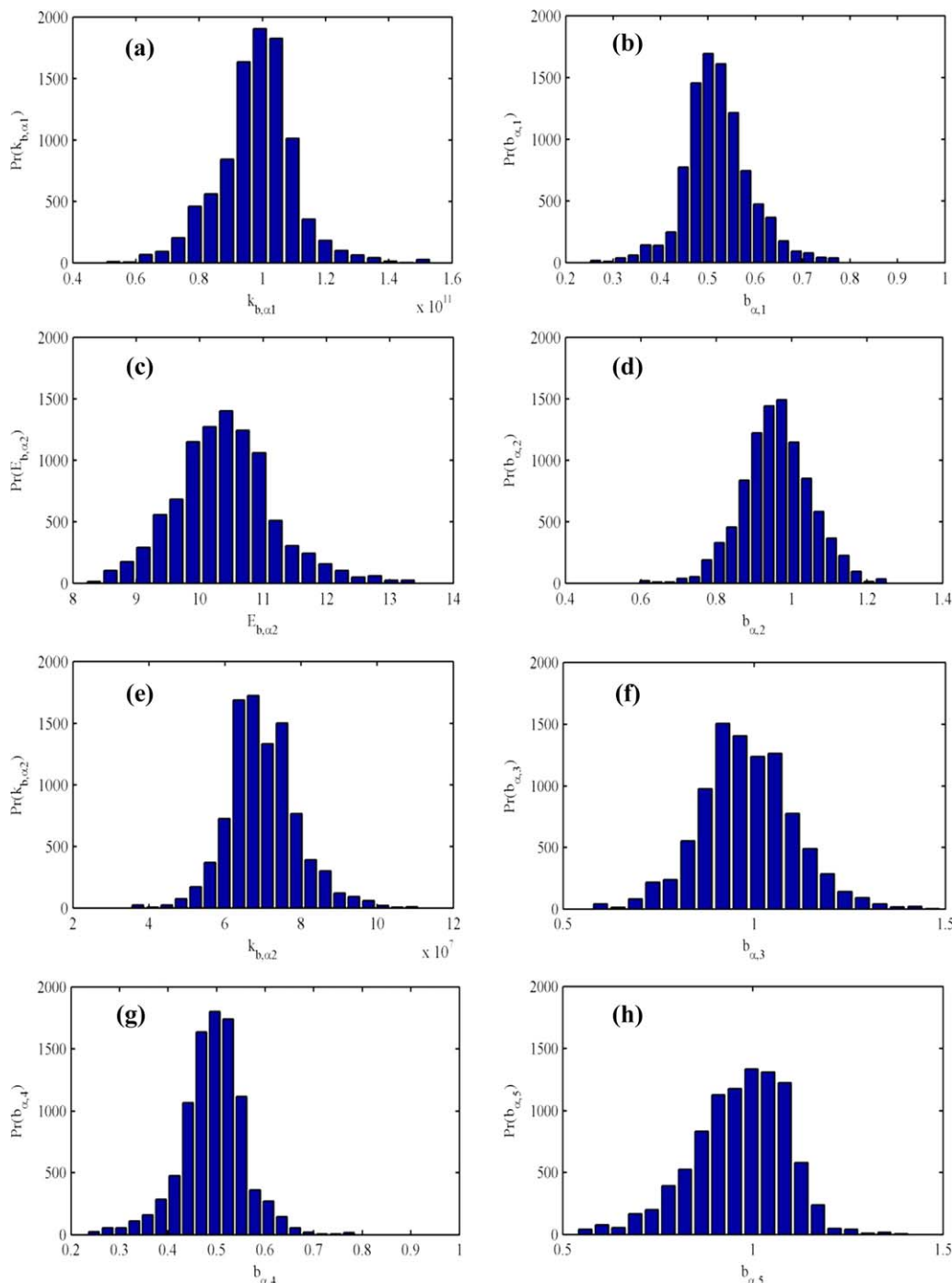


**Figure 3. The marginal distributions of parameters obtained for  $\alpha$ -form nucleation kinetics.**

[Color figure can be viewed in the online issue, which is available at [wileyonlinelibrary.com](http://wileyonlinelibrary.com).]

An informative prior distribution  $\Pr(\theta)$  that specifies the minimum and maximum possible values of  $\theta$  is used in this study

$$\Pr(\theta) \propto \begin{cases} 1 & \text{if } \theta_{\min} \leq \theta \leq \theta_{\max} \\ 0 & \text{otherwise,} \end{cases} \quad (41)$$

which means that all values of  $\theta$  between  $\theta_{\min}$  and  $\theta_{\max}$  have equal probability.

The product of the likelihood  $L(\theta|y)$  and prior distribution  $\Pr(\theta)$  specifies the Bayesian posterior, which is the joint probability distribution for all parameters after data have been observed. Once the Bayesian posterior is defined, Mar-

kov Chain Monte Carlo (MCMC) integration<sup>28</sup> was applied to compute the mean, mode, and credible intervals (aka Bayesian confidence intervals) associated with each of the parameters in an efficient manner.

The Markov chain is a sequence of random variables  $\theta^0, \theta^1, \dots$ , drawn from approximate distributions and then corrected to better approximate the Bayesian posterior distribution, for which, for any  $s$ , the distribution of  $\theta^{s+1}$  given all previous  $\theta^s$  depends only on the most recent value,  $\theta^s$ . During application, several parallel chains can be drawn. Parameters from each chain  $c$ ,  $\theta^{c,s}$ ,  $s = 1, 2, 3, \dots$ , are produced by starting at some point  $\theta^{c,0}$  and then, for each step

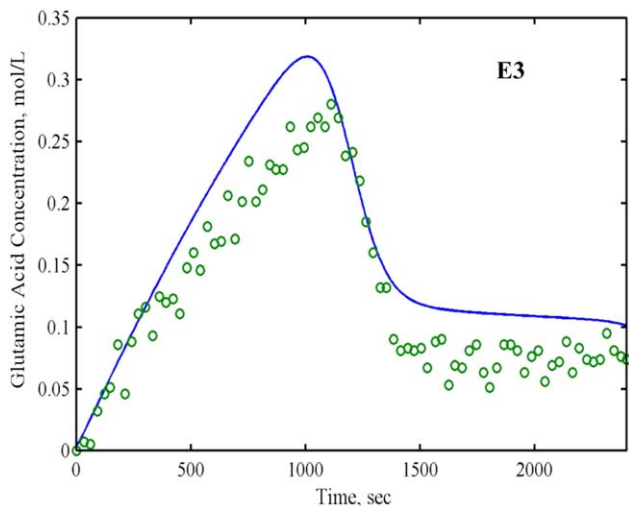


**Figure 4.** Comparison between the model predictions and experimental measurements for the glutamic acid concentration in Experiment E3 (solid line: model predictions; circles: experimental data from Ref. 30).

[Color figure can be viewed in the online issue, which is available at [wileyonlinelibrary.com](http://wileyonlinelibrary.com).]

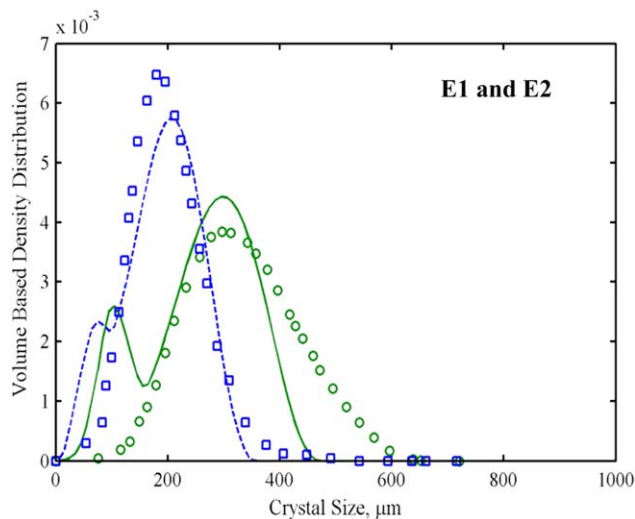


**Figure 5.** Comparison between the model predictions and experimental measurements for the crystal size distribution (lines: model predictions; markers: experimental data from Ref. 30; E1: solid line and circle; E2: dashed line and square).

[Color figure can be viewed in the online issue, which is available at [wileyonlinelibrary.com](http://wileyonlinelibrary.com).]

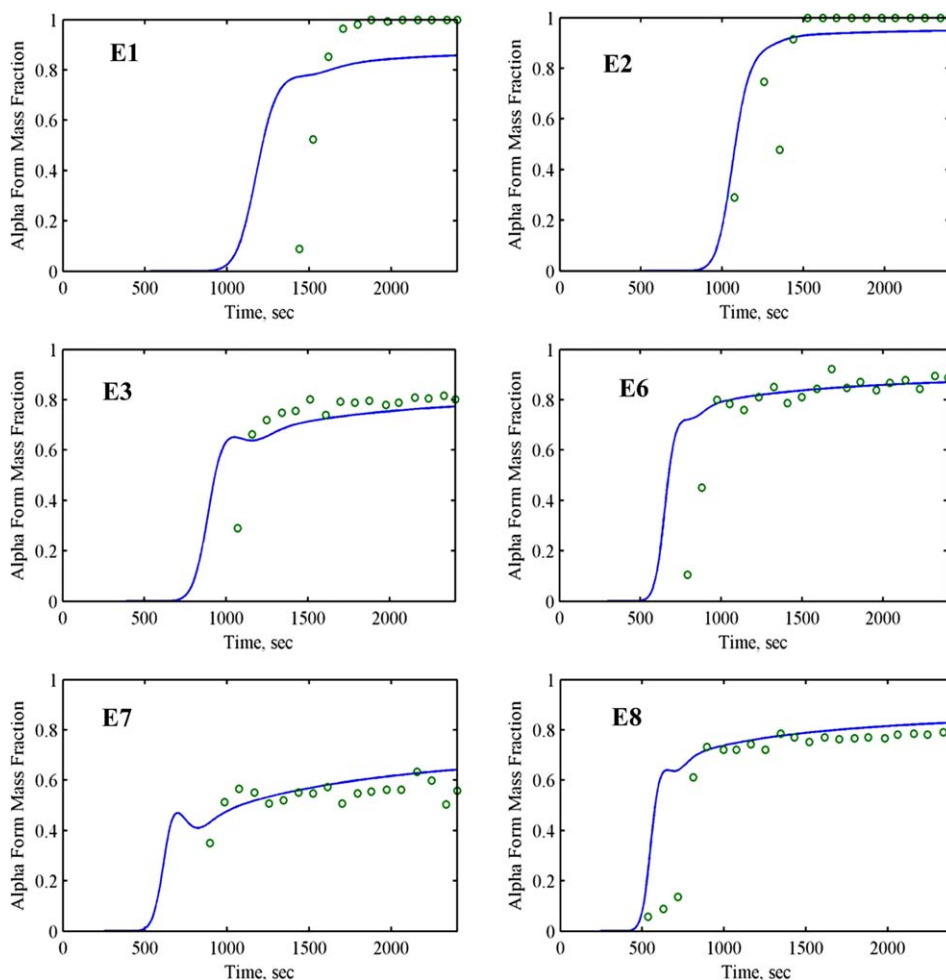


**Figure 6.** Comparisons between model predictions and experimental measurements for the  $\alpha$ -form polymorphic mass fraction (solid lines: model predictions; circles: experimental data from Ref. 30).

[Color figure can be viewed in the online issue, which is available at [wileyonlinelibrary.com](http://wileyonlinelibrary.com).]

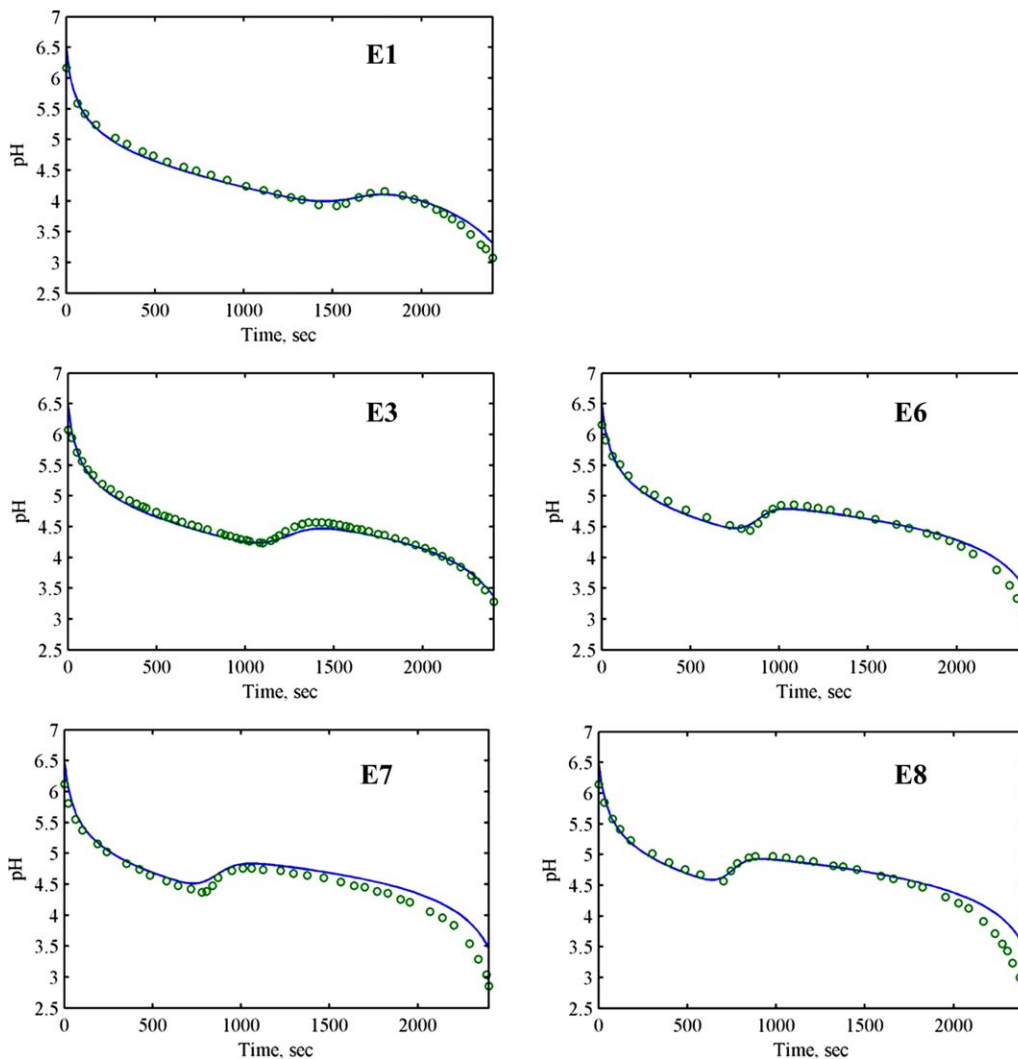


**Figure 7. Comparisons between model predictions and experimental measurement for the solution pH (solid lines: model predictions; circles: experimental data from Ref. 30).**

[Color figure can be viewed in the online issue, which is available at [wileyonlinelibrary.com](http://wileyonlinelibrary.com).]

s, drawing  $\theta^{c,s+1}$  from a jumping distribution  $T_s(\theta^{c,s+1}|\theta^{c,s})$  that depends on the previous draw,  $\theta^{c,s}$ . The jumping probability distributions must be constructed so that the Markov chain converges to the target posterior distribution. Here, the combination of differential evolution with MCMC

was adopted to construct the Markov chains.<sup>29</sup> For monitoring the convergence of the chains, potential scale reduction factors ( $\hat{R}_i$ ) were adopted to monitor the convergence of the Markov chains,<sup>28</sup> which are calculated from

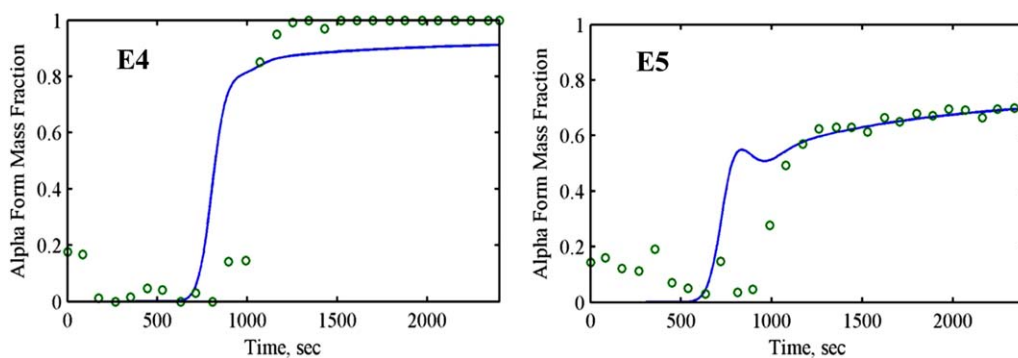


**Figure 8. Validation results for the  $\alpha$ -form polymorphic mass fraction (solid lines: model predictions; circles: experimental data from Ref. 30).**

[Color figure can be viewed in the online issue, which is available at [wileyonlinelibrary.com](http://wileyonlinelibrary.com).]

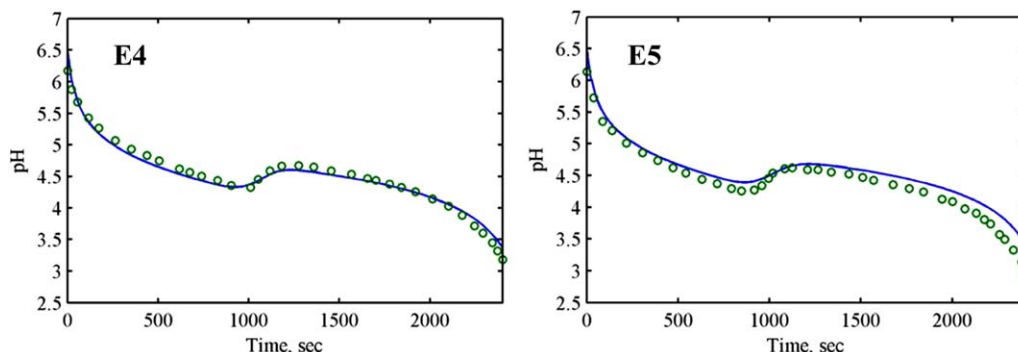


**Figure 9. Validation results for the solution pH (solid lines: model predictions; circles: experimental data from Ref. 30).**

[Color figure can be viewed in the online issue, which is available at [wileyonlinelibrary.com](http://wileyonlinelibrary.com).]

$$\hat{R}_i = \sqrt{\frac{v\hat{a}r^+(\theta|y)_i}{W_i}} \quad (42)$$

$$v\hat{a}r^+(\theta|y)_i = \frac{n-1}{n}W_i + \frac{1}{n}B_i \quad (43)$$

$$B_i = \frac{n}{m-1} \sum_{c=1}^m (\bar{\theta}_i^c - \bar{\theta}_i)^2 \quad (44)$$

$$W_i = \frac{1}{m} \sum_{c=1}^m (d_i^c)^2 \quad (45)$$

$$\bar{\theta}_i^c = \frac{1}{n} \sum_{s=1}^n \theta_i^{c,s} \quad (46)$$

$$\bar{\theta}_i = \frac{1}{m} \sum_{c=1}^m \bar{\theta}_i^c \quad (47)$$

$$(d_i^c)^2 = \frac{1}{n-1} \sum_{s=1}^n (\theta_i^{c,s} - \bar{\theta}_i^c)^2 \quad (48)$$

where  $\theta_i^{c,s}$  is the simulation draws of parameter  $i$  from step chain  $c$  at step  $s$ ,  $B_i$  and  $W_i$  are the between- and within-sequence variances of parameter  $i$ , respectively,  $m$  is the number of parallel chains, with each chain of length  $n$ . When  $\hat{R}_i$  is near 1 for all  $\theta_i$ , then the simulation is stopped and the probability distribution of each parameter can be observed by plotting the Markov chains in histograms, and the mean, mode, and credible intervals can be calculated accordingly.

## Results and Discussion

### Experimental data

The model parameters in the mathematical model of the previous sections were fit to some of the experimental data reported in the literature,<sup>30</sup> with the remaining data used for model validation. Other physical parameters for glutamic acid crystallization could be found in the literature.<sup>13</sup> For ease of reference, the experimental procedure conducted in the previous work<sup>30</sup> is briefly summarized here.

The precipitation experiments were performed in a 1-L jacketed crystallizer equipped with a thermostat and an overhead stirrer. The experiments were carried out in semibatch mode starting from 650 mL of initial solution of MSG in the crystallizer. During the precipitation, 320 mL of sulfuric acid solution with the same molarity as MSG was pumped into the crystallizer at a fixed flow rate of 8 mL/min. All experi-

ments were carried out at 25°C, and were monitored *in situ* using a pH meter, attenuated total reflection Fourier transform infrared (ATR-FTIR) spectroscopy, and a Raman immersion probe. The ATR-FTIR and Raman probes were used to measure the glutamic acid concentration and polymorphic mass fraction of the  $\alpha$ -form, respectively, throughout the batch. The size distribution of product crystals was determined at the end of each batch. Large fluctuations in the reported Raman measurement were observed for the first half of the batch, and the Raman measurement could be influenced by the size or the amount of crystals present in the solution. As a result, the fluctuated data were not used for parameter estimation. To achieve good fitting for the polymorphic purity experimental data, a mass concentration correction term,  $m_{\text{Raman}}$ , kg/m<sup>3</sup>, was used to calculate the  $\alpha$ -form polymorphic mass fraction,  $F_{m,\alpha}$

$$F_{m,\alpha} = \frac{m_\alpha}{m_\alpha + m_\beta + m_{\text{Raman}}} \quad (49)$$

There were eight sets of experimental data as summarized in Table 1, where six experiments (E1–E3 and E6–E8) were used to estimate the model parameters by Bayesian inference and the data from the remaining two experiments (E4 and E5) were used for validation.

### Parameter estimation

There are 29 model parameters to be estimated, which include 26 kinetic parameters, two power numbers for the impellers, and the aforementioned Raman correction term. Besides, four additional measurement noise parameters for pH, ATR-FTIR, Raman measurement, and crystal size distribution were also estimated (see Table 2). As all the experiments were conducted at constant temperature, the estimated kinetic parameters in crystallization mechanism (25), (27), (29), and (31) were  $k_{b,\alpha 1}$ ,  $k_{g,\alpha 1}$ ,  $k_{b,\beta 1}$ , and  $k_{g,\beta 1}$  instead. Table 2 shows the mean, mode, and 95% credible intervals of the estimated parameters obtained by Bayesian inference. For the sake of limited space, only the marginal probability distributions of the estimated parameters for the  $\alpha$ -form nucleation kinetics are shown in Figure 3. These distributions can be incorporated into model predictive control and other control algorithms that have been designed to be robust to stochastic parameter uncertainties.<sup>31</sup>

The initial parameters for the Markov chains were first obtained by minimizing the weighted difference between the experimental measurements  $y_{jk}$  and model predictions  $\hat{y}_{jk}$

$$J = \min_{\theta_{\text{sys}}} \sum_{j=1}^{N_m} \sum_{k=1}^{N_{d_j}} \frac{w_q}{N_{d_j}} (y_{jk} - \hat{y}_{jk}(\theta_{\text{sys}}))^2 \quad (50)$$

where  $w_q$  is a weighting factor that is the inverse of an estimate of the error variance  $\sigma_j^2$ . Initially,  $\sigma_j$  was set to the standard deviation of the actual measurement. A set of parameters were then estimated by solving the optimization problem (50). The standard deviations for the errors in the  $j$ th measured variable were estimated and used as  $\sigma_j$  to iteratively solve the parameter estimation optimization until no significant difference between the given and estimated standard deviations was detected.<sup>32</sup>

Figures 4–7 compare model predictions, using the mode estimates of the parameters in Table 2, with the experimental data used in fitting the model parameters. For the glutamic acid concentration measurement given in Experiment E3 in Figure 4, the solute concentration reflects the combined effects of the solute generation, dilution, and lumped depletion due to the nucleation and growth of the  $\alpha$  and  $\beta$  polymorphs. The steep decrease of the solute concentration after 1000 s is in correspondence to the sharp increase of the  $\alpha$ -form polymorph mass fraction in Figure 6 (E3) and the increase in pH for a short period of time displayed in Figure 7 (E3). In addition, dome-shaped concentration profiles as seen in Figure 4 and similar CSD results as observed in Experiments E1 and E2 of Figure 5 were observed in the other experiments. The change in the stirring rate from 250 to 500 rpm resulted in stronger secondary nucleation in Experiment E2 than E1, as indicated in nucleation kinetics (24) and (28), which made the crystal size distribution shift to the smaller size range, as shown in Figure 5. Similar results were obtained for the other experiments that had high stirring rate.

As in Figure 5, the predicted CSDs are bimodal, whereas the experimental CSD are unimodal. The small peak of the predicted crystal size distribution at less than 100  $\mu\text{m}$  for E2 in Figure 5 is too small to be observable within the accuracy of a CSD measurement. For E1, the first peak of the predicted crystal size distribution occurs at about 100  $\mu\text{m}$ . The particle size distributions were experimentally determined by Ref. 30 after the crystals were filtered and dried,<sup>33</sup> and the images in Figure 4 of Ref. 30 show a population of much smaller crystals adhered to the surface of larger crystals, but such a smaller population of crystals does not appear in the experimental CSD data in Figure 10 of Ref. 30 that were used in this study and partly shown in Figure 5. Smaller crystals often have a tendency to stick to the surface of larger crystals, which would cause any small crystals associated with the first peak in the CSD to show up in the measured CSD of Ref. 30 as parts of larger crystals.<sup>8</sup> Such a systematic experimental bias in the CSD measurements would explain both why our mathematical model predicts a higher amount of small crystals than reported in the CSDs in Ref. 30 and predicts a smaller amount of the largest crystals than reported in the CSDs in Ref. 30. Potential biases in measured crystal size distributions are well established in the literature.<sup>34–36</sup>

Although only one solute concentration profile in Experiment E3 was used in parameter estimation, this limitation in the data could be compensated by the use of pH measure-

ment as pH is tightly coupled to the glutamic acid concentration in the range of pH in the experiments, which is clear from Figure 1 and reactions (1)–(3).

### Model validation

With the mode estimates of the parameters in Table 2, validation of the developed model using the datasets from Experiments E4 and E5 are provided in Figures 8 and 9. The data from Experiments E4 and E5 were not used in the above parameter estimation, and the experimental conditions are different from Experiments E3 and E6 in the stirring rate and impeller type used, respectively. The  $\alpha$ -form mass fraction in Experiments E4 and E5 have a high degree of fluctuation in the first half of the batch which is why Eq. 49 used to alleviate this data limitation. The rather precise pH measurements in both experiments are very well predicted by the model (see Figure 9). The good agreement of the validation results shown in Figures 8 and 9 provides some confidence that the first-principles model of pH-shift reactive crystallization can be used in process control studies, as long as the control systems are designed to be reasonably robust to model uncertainties.

### Conclusions

A mathematical model is developed for the semibatch pH-shift reactive crystallization of L-glutamic acid, taking into account the species balance of the glutamic-related ions, nonideal solution properties, polymorphic crystallization kinetics, mixing effects, and population balances of the solute crystals. For the population balance model, a finite-volume method is used to reduce the PDEs into a set of ODEs that are then solved together with the nonlinear algebraic equations for the species balances. Experimental data from literature are used to estimate the model parameters using Bayesian inference. The agreement between the experimental data and the predicted outputs of the resulting mathematical model is sufficiently good to justify the use of the model in process control studies.

### Literature Cited

- Cisternas LA, Vásquez CM, Swaney RE. On the design of crystallization-based separation processes: review and extension. *AIChE J.* 2006;52:1754–1769.
- Mangin D, Puel F, Veesler S. Polymorphism in processes of crystallization in solution: a practical review. *Org Process Res Dev.* 2009; 13:1241–1253.
- Randolph AD, Larson MA. *Theory of Particulate Processes: Analysis and Techniques of Continuous Crystallization*. San Diego: Academic Press, 1988.
- Black SN, Davey RJ. Crystallization of amino acids. *J Cryst Growth.* 1988;90:136–144.
- Zhu J, Garside J. Controlled batch crystallization by pH variation. *The 1997 Jubilee Research Event, Vol. 1–2*. Rugby, UK: Institution of Chemical Engineers, 1997:449–452.
- Borissova A, Jammao Y, Javed KH, Lai X, Mahmud T, Penchev R, Roberts KJ, Wood W. Modeling the precipitation of L-glutamic acid via acidification of monosodium glutamate. *Cryst Growth Des.* 2005; 5:845–854.
- Box GEP, Draper NR. The Bayesian estimation of common parameters from several responses. *Biometrika.* 1965;52:355–365.
- Duran MA, White BS. Bayesian estimation applied to effective heat transfer coefficients in a packed bed. *Chem Eng Sci.* 1995;50:495–510.
- Bois FY, Fahmy T, Block JC, Gatel D. Dynamic modeling of bacteria in a pilot drinking-water distribution system. *Water Res.* 1997;31: 3146–3456.
- Coleman MC, Block DE. Bayesian parameter estimation with formative priors for nonlinear systems. *AIChE J.* 2006;52:651–667.

<sup>8</sup>It is challenging to quantify a population of small crystals stuck to the surfaces of a much larger population of large crystals.

11. Pouillot R, Albert I, Cornu M, Denis JB. Estimation of uncertainty and variability in bacterial growth using Bayesian inference. Application to *Listeria monocytogenes*. *Int J Food Microbiol*. 2003;81:87–104.
12. Gunawan R, Jung MY, Seebauer EG, Braatz RD. Maximum a posteriori estimation of transient enhanced diffusion energetics. *AIChE J*. 2003;49:2114–2122.
13. Hermanto MW, Kee NC, Tan RBH, Chiu MS, Braatz RD. Robust Bayesian estimation of kinetics for the polymorphic transformation of L-glutamic acid crystals. *AIChE J*. 2008;54:3248–3259.
14. Alatalo H, Hatakka H, Kohonen J, Reinikainen S, Louhi-Kultanen M. Process control and monitoring of reactive crystallization of L-glutamic acid. *AIChE J*. 2010;56:2063–2076.
15. Alatalo H, Kohonen J, Qu H, Hatakka H, Reinikainen SP, Louhi-Kultanen M, Kallas J. In-line monitoring of reactive crystallization process based on ATR-FTIR and Raman spectroscopy. *J Chemom*. 2008;22:644–652.
16. Nagy ZK, Fujiwara M, Braatz RD. Modelling and control of combined cooling and antisolvent crystallization processes. *J Process Control*. 2008;18:856–864.
17. Prausnitz JM, Lichtenthaler RN, de Azevedo EG. *Molecular Thermodynamics of Fluid-Phase Equilibria*. New Jersey: Prentice Hall PTR, 1999.
18. Togkalidou T, Tung HH, Sun Y, Andrews AT, Braatz RD. Parameter estimation and optimization of a loosely bound aggregating pharmaceutical crystallization using in situ infrared and laser backscattering measurements. *Ind Eng Chem Res*. 2004;43:6168–6181.
19. Kee NCS, Tan RBH, Braatz RD. Selective crystallization of the metastable  $\alpha$ -form of L-glutamic acid using concentration feedback control. *Cryst Growth Des*. 2009;9:3044–3051.
20. Schöll J, Vicum L, Müller M, Mazzotti M. Precipitation of L-glutamic acid: determination of nucleation kinetics. *Chem Eng Technol*. 2006;29:257–264.
21. Lindenberg C, Schöll J, Vicum L, Mazzotti M, Brozio J. L-glutamic acid precipitation: agglomeration effects. *Cryst Growth Des*. 2008;8:224–237.
22. Cornel J, Lindenberg C, Mazzotti M. Experimental characterization and population balance modeling of the polymorph transformation of L-glutamic acid. *Cryst Growth Des*. 2009;9:243–252.
23. Mesbah A, Kramer HJM, Huesman AEM, Van den Hof PMJ. A control oriented study on the numerical solution of the population balance equation for crystallization processes. *Chem Eng Sci*. 2009;64:4262–4277.
24. Koren B. A robust upwind discretization method of advection, diffusion and source terms. In: Vreugdenhill CB, Koren B, editors. *Numerical Methods for Advection-Diffusion Problems*. Braunschweig: Vieweg Verlag, 1993:117–138.
25. Qamar S, Elsner MP, Angelov IA, Warnecke G, Seidel-Morgenstern A. A comparative study of high resolution schemes for solving population balances in crystallization. *Comput Chem Eng*. 2006;30:1119–1131.
26. Bretthorst GL. An introduction to parameter estimation using Bayesian probability theory. In: Fougere PF, editor. *Maximum Entropy and Bayesian Methods*. Dordrecht: Kluwer Academic Publishers, 1990:53–79.
27. Carlin BP, Louis TA. *Bayes and Empirical Bayes Methods for Data Analysis*. Boca Raton: Chapman & Hall/CRC, 2000.
28. Gelman A, Carlin JB, Stern HS, Rubin DB. *Bayesian Data Analysis*. New York: Chapman & Hall/CRC, 2004.
29. Ter Braak CJ. A Markov Chain Monte Carlo version of the genetic algorithm differential evolution: easy Bayesian computing for real parameter spaces. *Stat Comput*. 2006;16:239–249.
30. Qu H, Alatalo H, Hatakka H, Kohonen J, Louhi-Kultanen M, Reinikainen SP, Kallas J. Raman and ATR FTIR spectroscopy in reactive crystallization: simultaneous monitoring of solute concentration and polymorphic state of the crystals. *J Cryst Growth*. 2009;311:3466–3475.
31. Nagy ZK, Braatz RD. Worst-case and distributional robustness analysis of finite-time control trajectories for nonlinear distributed parameter systems. *IEEE Trans Control Syst Technol*. 2003;11:694–704.
32. Kee NCS, Tan RBH, Braatz RD. Semiautomated identification of the phase diagram for enantiotropic crystallizations using ATR-FTIR spectroscopy and laser backscattering. *Ind Eng Chem Res*. 2011;50:1488–1495.
33. Hatakka H, Alatalo H, Louhi-Kultanen M, Lassila I, Hægström E. Closed-loop control of reactive crystallization PART II: polymorphism control of L-glutamic acid by sonocrystallization and seeding. *Chem Eng Technol*. 2010;33:751–756.
34. Rawlings JB, Miller SM, Witkowski WR. Model identification and control of solution crystallization processes—a review. *Ind Eng Chem Res*. 1993;32:1275–1296.
35. Loizeau JL, Arbouille D, Santiago S, Vernet JP. Evaluation of a wide-range laser diffraction grain-size analyzer for use with sediments. *Sedimentology*. 1994;41:353–361.
36. Abbas A, Nobbs D, Romagnoli JA. Investigation of on-line optical particle characterization in reaction, and cooling crystallization systems—current state of the art. *Meas Sci Technol*. 2002;13:349–356.

Manuscript received Sept. 25, 2012, and revision received Mar. 24, 2014.